Smart Materials in Medicine 5 (2024) 196–206

Contents lists available at ScienceDirect

Smart Materials in Medicine

journal homepage: www.keaipublishing.com/en/journals/smart-materials-in-medicine/

A magnetic-enhanced FRET biosensor for simultaneous detection of multiple antibodies

Lihua Li [a], Yao Lu [b], Xinyue Lao [a], Sin-Yi Pang [a], Menglin Song [a], Man-Chung Wong [a], Feng Wang [c], Mo Yang [d], Jianhua Hao [a,*]

[a] Department of Applied Physics, The Hong Kong Polytechnic University, Hong Kong, PR China
[b] Clinical Research Center, Department of Joint and Orthopedics, Orthopedic Center, Zhujiang Hospital, Southern Medical University, Guangzhou, Guangdong, 510282, PR China
[c] Department of Materials Science and Engineering, City University of Hong Kong, Hong Kong, PR China
[d] Department of Biomedical Engineering, The Hong Kong Polytechnic University, Hong Kong, PR China

ARTICLE INFO

Keywords:
Upconversion nanoparticles
IgG and IgM detection
SARS-CoV-2 antibodies
Multicolor detection
Magnetic nanocrystals

ABSTRACT

Accurate, rapid and sensitive detection of specific immunoglobulin G (IgG) and immunoglobulin M (IgM) antibodies in human samples is crucial for preventing and assessing pandemics, especially in the case of recent COVID-19 outbreaks. However, simultaneous and efficient detection of IgG and IgM in a single system remains challenging. Herein, we developed a multicolor nanosystem capable of quantitatively analyzing *anti*-SARS-CoV-2 IgG and IgM with high sensitivity within 20 min. The detection system consists of core-shell upconversion nanoparticles (csUCNPs), secondary antibodies labeled with fluorescent dyes (sab), and magnetic nanocrystals (PMF). By leveraging the Förster resonance energy transfer (FRET) effect, the photoluminescence (PL) intensity of blue and green regions is restored for IgG and IgM detection, respectively. Inspiringly, owing to the introducing of PMF, the limits of detection (LODs) of IgG and IgM tested are improved to 89 fmol L^{-1} and 19.4 fmol L^{-1}, representing about 416-folds and 487-folds improvement over only-dye dependent system, respectively. Mechanistic investigations reveal that the high collective effect and surface energy transfer efficiency from csUCNPs to PMF contribute to the enhanced detection sensitivity. The assay enables us to quantify clinical vaccinated samples with high specificity and precision, suggesting our multicolor platform can be a promising alternative for clinical point-of-care serological assay.

1. Introduction

Viral infections, such as Ebola virus, influenza virus, and recently SARS-CoV-2 virus, pose significant threats to human life and health, leading to high morbidity and mortality. The rapid and sensitive detection of antibodies/antigens is crucial for global public health and prevention of pandemic. Currently, various vaccines have been developed to combat the severe COVID-19 pandemic caused by SARS-CoV-2 [1]. Monitoring the real-time SARS-CoV-2 infection and assessing vaccine efficacy rely on the detection of saliva [2] and serological antibodies, which are closely related to immune response and antibody titers [3]. Additionally, antibody quantification plays a vital role in determining the epidemic prevention policy [4]. Detecting antibodies at early stages with low antibody concentrations can effectively diagnose viral infections [5], offering an alternative to qRT-PCR test due to the high stability of antibodies [6,7]. Serological analysis also helps track therapeutic development, individual immune responses [8], as well as evaluate the potential of neutralizing antibodies as antiviral agents and prophylactics [9]. Specifically, the simultaneous or sequential occurrence of specific anti-viral immunoglobulin-M (IgM) and immunoglobulin-G (IgG) in serum makes them important serological indicators for early infection. However, the current detection of IgM and IgG are always carried out in separate and independent procedure, and most of the works focus on detection of IgG [10], which cannot satisfy the monitoring and evaluation of infection [11]. Therefore, there is a great need to develop a highly accurate, sensitive, and straightforward method that can detect IgM and IgG antibodies against SARS-CoV-2 simultaneously, with potential for broader applications.

Strenuous efforts have been devoted to developing antibody tests, including the enzyme-linked immunosorbent assays (ELISA) [12], lateral

* Corresponding author.
E-mail address: jh.hao@polyu.edu.hk (J. Hao).

https://doi.org/10.1016/j.smaim.2023.12.003
Received 6 November 2023; Received in revised form 26 December 2023; Accepted 29 December 2023
Available online 6 January 2024

flow assays [13], chemiluminescent microparticle immunoassays [14], and field-effect transistors [15]. Among these methods, immunoassays are the most reliable, but they require trained professionals and have longer turnaround times, ranging from hours to days, for obtaining results. Lateral flow assays can provide quick results within minutes and user friendly. In addition, both immunoassays and lateral flow assays lack of sufficient sensitivity. Moreover, IgG and IgM detection is not performed simultaneously, resulting in expensive and complex clinical procedures that are not conducive to infection control and clinical assay. Researchers have recently raised new protocols for viral RNA and antibody detection, such as immuno-PCR method [16] and multiplex microfluidic electrochemical sensors [17]. However, the design and implementation are both complicated, making them impractical for point-of-care detection and application. Therefore, it remains critical to develop rapid and sensitive approaches for detecting IgG and IgM antibodies simultaneously.

Upconversion nanoparticles (UCNPs) enjoying high photostability, non-autofluorescence, non-photobleaching and long lifetime, have intrigued great attention in biodetection [18–20]. UCNPs are capable of absorbing two or more low-energy photons (near-infrared (NIR) light) and subsequently emit one high-energy photon in the UV, visible and NIR ranges. This characteristic eliminates background interference and facilitates ultrasensitive biodetection [21]. Notably, the multiple narrow emissions enable the simultaneous detection of multiple biotargets.

Förster resonance energy transfer (FRET) is a non-radiatively energy transfer from a fluorescent donor to an acceptor with close distance (2–10 nm), which is particularly suitable for RNA, protein, polypeptide and polynucleotide detection [22,23]. UCNPs are often functioned as donors because of their sharp emission peak, tunable emission wavelength, and large anti-Stokes shift [24]. Energy acceptors, including organic dyes, Au nanoparticles, graphene oxide, and quantum dots [25], share a common characteristic: their absorption wavelength overlaps well with the emission peak. The FRET-based detection systems have some drawbacks including insufficient sensitivity to detect targets due to incomplete spectra matching and the inability to capture targets effectively. However, magnetic NPs have the potential to significantly enhance detection sensitivity by binding and gathering the targets [26, 27]. Furthermore, a well-designed magnetic NP could also reinforce the spectra quenching effect.

Here, we develop a platform that combines multicolor core-shell UCNPs (csUCNPs) as donors and secondary antibodies labeled with dyes (sab) as acceptors. This platform enables the simultaneous detection of immunoglobulin M (IgM) and immunoglobulin G (IgG) antibodies against SARS-CoV-2 in a single system. Through the rational design of $NaYF_4$,Yb/Tm@$NaYF_4$ and $NaYF_4$,Yb/Er@$NaYF_4$ csUCNPs, the emission of csUCNPs at 475 nm and 542 nm could be quenched by FITC-antiIgG and Cy5.5 PE-antiIgM, respectively. In addition, there is neglectable fluorescence of FITC could be detected at ~540 nm because of non-radioactive energy transfer in FITC, which in turn ensure the high accuracy for IgM detection. Furthermore, in order to enhance the quenching efficiency and improve the detection sensitivity, we have introduced magnetic PEI-$MnFe_2O_4$ nanoparticles (PMF NPs) to capture and enrich the targets. As a result, the limits of detection (LOD) for IgM and IgG have been improved to 13.49 and 17.50 pg mL^{-1} respectively. This represents a remarkable improvement of 416-fold and 487-fold for IgG and IgM detection, respectively. Moreover, the entire detection process can be completed within 20 min, which is superior to most commercial immunoassays. Therefore, our work has established a highly sensitive, specific and rapid method for the detection of IgG and IgM antibodies.

2. Experiments

2.1. Experimental section

2.1.1. Synthesis of $NaGdF_4$:Yb/Tm and $NaGdF_4$:Yb/Er[1]

The preparation of core UCNP and core-shell UCNP was performed according to the previous study [1]. Briefly, 1 mL $Gd(CH_3CO_2)_3{\cdot}xH_2O$ (0.2 M), 0.98 mL $Yb(CH_3CO_2)_3{\cdot}xH_2O$ (0.2 M), 20 μL $Tm(CH_3CO_2)_3{\cdot}xH_2O$ solution were added to 4 mL oleic acid and 6 mL 1-octadenece in a 50 mL round bottle flask, the mixture was heated up to 150 °C and kept for 40 min to evaporate the excess water in the solution, the mixture turned light yellow. After cooling down to temperature slowly, 1 mL NaOH (1 M in methanol) and 3.3 mL NH_4F (0.4 M in methanol) were mixed for 10 s and subsequantly added to the above solution with constant stirring. The mixture was further programmed to heat up to remove the excess methanol and kept at 280 °C for 90 min to form the core nanocrystals. The core UCNPs were washed with methanol and cyclohexane for several times and stored in a glass bottle using cyclohexane for further use. Similarly, $NaGdF_4$:Yb/Er NPs were synthesized using the same protocol with a different solution: 1.56 mL $Gd(CH_3CO_2)_3{\cdot}xH_2O$ (0.2 M), 0.4 mL $Yb(CH_3CO_2)_3{\cdot}xH_2O$ (0.2 M), 40 μL $Er(CH_3CO_2)_3{\cdot}xH_2O$.

2.1.2. Synthesis of $NaGdF_4$:Yb/Tm@$NaGdF_4$ and $NaGdF_4$:Yb/Er@$NaGdF_4$ core-shell structure

For the synthesis of core-shell structure of csUCNPs, 2 mL $Gd(CH_3CO_2)_3{\cdot}xH_2O$ (0.2 M) was added to 4 mL oleic acid and 6 mL 1-octadenece in a 50 mL round bottle flask and the process was the same as the core UCNP to evaporate excess water. At room temperature, the stock core NaGdF4:Yb/Tm UCNP was added to the solution and subsequently 1 mL NaOH (1 M in methanol) and 3.3 mL NH_4F (0.4 0 M in methanol) were added to the above mixture with constant stirring. Then the mixture was programmed to heat up to remove the excess methanol and kept at 280 °C for 90 min to form the cs-UCNP nanocrystals.

2.1.3. Preparation of ligand-free csUCNPs

After synthesizing the oleic acid csUCNPs, they were dispersed in 15 mL ethanol along with 112 μL HCl. The mixture was then subjected to ultrasonication for 30 min. Subsequently, the treated csUCNPs were separated by centrifugation. The resulting pellet was redispersed in 15 mL ethanol containing 11.2 μL HCl and subjected to another round of ultrasonication for 30 min. The final csUCNP products were obtained by centrifugation, followed by washing with water and ethanol several times. Finally, the csUCNPs were redispersed in water and ready for further use.

2.1.4. Modification of csUCNPs

The ligand free csUCNPs were co-cultured with PAA solution to modify carboxylic groups on their surface as previously described [28]. Then the csUCNPs were conjugated with nucleocapsid protein using the typical NHS/EDC method. The csUCNPs with carboxyl (0.1 g mL^{-1}) were activated in a mixture of EDC (20 mg/mL) and NHS (10 mg/mL) for1 hour at room temperature in dark. Then the SARS-CoV-2 nucleocapsid protein solution (1 μM in 10 mM PBS solution, 2 μl) were added to the above solution at 4 °C with constant stirring overnight. Afterward, the csUCNPs were treated with MEA (1 M, in 10 mM PBS solution) for 1 h to eliminate the unreacted carboxylic groups and centrifuged to remove the impurites. Moreover, the protein isoelectric point (PI) of SARS-CoV-2 nucleocapsid protein is above 11, thus the *N*-csUCNPs are positively charged [29] in physiological conditions.

2.1.5. Synthesis of $MnFe_2O_4$ magnetic nanoplates

0.02 mol $MnCl_2$ (5 g) and 0.03 mol $FeCl_3$ (8.1 g) were dispersed in 100 mL dd H_2O with continuous stirring, the solution was heated to 70 °C. Subsequently, 70 mL 6 M NaOH was added to the above mixture, and the solution was kept agitated at 70 °C for 1.5 h, the product $MnFe_2O_4$ were separated from centrifugation (8000 rpm, 10 min) and washed with abundant water for several times to get rid of the extra NaOH. For the fabrication of PEI-capped $MnFe_2O_4$ NPs (MF NPs), 100 mg $MnFe_2O_4$ were dispersed in 20 mL dd H_2O, then 0.2 g PEI (mw = 25 kDa) was added to the solution with agitation at room temperature for 24 h, then washed with water for 3 times to get rid of the abundant PEI. The final products were termed as PMF.

2.1.6. Preparation of PMF-sab

100 μL PMF (100 μg mL^{-1}) were co-cultured with 10 μL FITC-*anti*-IgG (100 μg mL^{-1}) and PE-Cy5.5-*anti*-IgM (100 μg mL^{-1}) at 4 °C for 12 h, respectively. Afterward, the samples were washed using ddH_2O for 3 times and blocked with 1 % bovine serum albumin (BSA) for 2 h. Finally, the PMF-sab samples were centrifuged, resuspended in PBS, and stored at 4 °C for next use.

2.1.7. FRET efficiency

According to Förster's quantitative theory, the spectral overlap and intermolecular distance are key factors for LERE efficiency and the universal equation for FRET efficiency is as follows:

$$E = \frac{1}{1 + \left(\frac{R}{R_0}\right)^6} \quad (1)$$

when the transfer efficiency is 50 %, a fluorescent distance between donors and acceptors is defined as R_0. Where R is the distance between donors and acceptors. There is an inverse relationship between energy transfer efficiency E and distance between donors and acceptors. The transfer rate is about to reach its maximum.

2.1.8. Theoretical interpretation

The manuscript utilizes the finite-difference time-domain (FDTD) method with the FDTD-Solutions software developed by Lumerical Inc. The simulations in this study involve models of NaYF4:Yb/Er@NaYF4, PMF, and IgM., the organic Cy5.5 PE here are exclude from the simulations because of negligible size. The quenching efficiency of a single emitter is evaluated by analyzing the change in emission enhancement (or quenching), I/I0, which is directly related to the alteration of its quantum yield. The specific formula for calculating this relationship is as follows:

$$Q_{er} = 1\text{-}\frac{I}{I_0} \quad (2)$$

$$\frac{I}{I_0} = \frac{\eta}{\eta_0} = \frac{\Gamma_R/\Gamma_R^0}{(\Gamma_R/\Gamma_R^0 + \Gamma_{NR}/\Gamma_R^0)\eta_0 + 1\text{-}\eta_0} \quad (3)$$

Where Γ_R^0 is the original radiative decay rate without PMF and dyes, Γ_R is the total decay rates, Γ_{NR} is the non-radiative decay rates, η (η0) represents the intrinsic quantum yields of the emitter in the presence PMF with and without IgG. The detailed method was according to previous research [30].

2.1.9. Detection of samples

Gradient concentrations (0, 1, 2, 4, 8, 16, 32 ng mL^{-1}) of IgG and IgM were added to the negative serum samples, then the serum samples were co-cultured with PMF-sab for 20 min at 37 °C, the samples were further gathering using a magnetic to get rid of the supernatant. And then the samples were mixed with ($NaYF_4$,Yb,Tm@$NaYF_4$ + $NaYF_4$,Yb,Er@$NaYF_4$ solution and detected under 980 nm laser excitation.

The detection of limit (LOD) was calculated as below:

$$LOD = \frac{3Sa}{b} \quad (4)$$

Where *Sa* is the standard deviation of the response and b is the slope of the calibration curve.[2]

2.1.10. Ethical statements

This study was approved by the I Clinical Research Center of Zhujiang Hospital, Southern Medical University, (Guangzhou, China) [No. 2022-KY-253-01]. All participants have signed written informed consent.

2.1.11. Clinical sample detection

4 COVID-19 negative persons (not vaccinated, no infection history), 16 patients vaccinated CoronaVac more than 1 year, 10 patients vaccinated CoronaVac in recent 6 months were from Zhujiang Hospital. About 10 μL plasma were diluted with 1 mL PBS and then mixed with the magnetic PMF-sab, the detection procedure was similar with the "detection of samples".

3. Results and discussion

3.1. Main design of UCNP-biosensors

Herein, we propose a homogeneous for simultaneous detection of IgG and IgM using a csUCNP biosensor, PMF-dye-labeled secondary antibody (sab) for detecting IgG and IgM simultaneously (Scheme 1). Initially, highly electropositive PMF is loaded with FITC-antiIgG and Cy5.5 PE-antiIgM *via* electronic attraction. The loaded PMF is then blocked with bovine serum albumin (BSA) to create PMF-FITC-sab and PMF-Cy5.5 PE-sab in Scheme 1. The serum samples collected from COVID-19 patients are co-cultured with PMF-FITC-sab and PMF-Cy5.5 PE-sab to capture the target antibodies. Subsequently, $NaYF_4$,Yb/Tm@$NaYF_4$ and $NaYF_4$,Yb/Er@$NaYF_4$, which exhibit multicolor (blue and green) luminescence emission, are added to the mixture as energy donors for FRET. The presence of IgG and IgM in the serum lead to a significant increment in distance, thus blocking the energy transfer from UCNP to PMF-FITC and PMF-Cy5.5, resulting in the recovery of the PL of UCNP.

3.2. Synthesis and optimization of csUCNPs

The emission intensities and locations of peaks of UCNPs are highly related to the composition, core-shell structure and host matrix. In order to identify the optimal UCNPs for further detection, we designed and synthesized typical Tm and Er doped $NaYF_4$ and $NaGdF_4$ hosts, which commonly used in various applications. For characterization purposes, we select Tm-doped $NaYF_4$ and $NaGdF_4$ hosts as representative examples. To prevent nonspecific quenching and enhance the stability of the lanthanide ions (Ln^{3+}), csUCNPs were designed and synthesized. Transmission electron microscopy (TEM) images of $NaYF_4$,Yb/Tm and core-shell $NaYF_4$,Yb/Tm@$NaYF_4$ are seen in Fig. 1a and b, confirming their high monodispersity. The X-ray powder diffraction (XRD) patterns of the core $NaYF_4$,Yb/Tm and core-shell $NaYF_4$,Yb/Tm@$NaYF_4$ correspond well with the standard hexagonal-phase $NaYF_4$ (PDF 28–1192) (Fig. 1c). In addition, the $NaGdF_4$,Yb/Tm and core-shell $NaGdF_4$,Yb/Tm@$NaGdF_4$ NPs have also been characterized using TEM and XRD, and exhibited a typical hexagonal-phase structure as observed in Fig. 1d, e and f. Magnetic $MnFe_2O_4$ nanoplates feature a cubic-like morphology with the particle size of 110 nm, and the XRD pattern confirms the crystalline phase and purity of the samples (Fig. 1h). The ferromagnetic properties of $MnFe_2O_4$ were confirmed through measurements using a vibrating sample magnetometer (VSM) (Fig. S1), indicating their capability in magnetic separation and target enrichment. In Fig. 1i, the absorption spectrum of FITC-antiIgG overlaps well with the emission of Tm ion at blue region (450–475 nm), while that absorption spectrum of Cy5.5 PE-IgM overlaps well with the emission of Er ion at 542 nm. The above results indicate the possibility of FRET process from UCNPs to the dye molecules.

3.3. Performance of csUCNPs in IgG and IgM detection

Due to the energy transfer from Yb^{3+} to Tm^{3+} and Er^{3+} (Fig. 2a), $NaYF_4$/Yb,Tm@$NaYF_4$ and $NaYF_4$/Yb,Er@$NaYF_4$ emit characteristic blue and green luminescence, respectively, and the PL intensity in $NaYF_4$ host is stronger than that of $NaGdF_4$ host at the same concentration (Fig. 2b and c). The $NaYF_4$/Yb,Tm@$NaYF_4$ emit typical blue luminescence of Tm^{3+} at 450 nm ($^1D_2 \rightarrow {}^3F_4$) and 475 nm ($^1G_4 \rightarrow {}^3H_6$) upon 980 nm excitation. By contrast, $NaYF_4$/Yb,Er@$NaYF_4$ exhibit characteristic

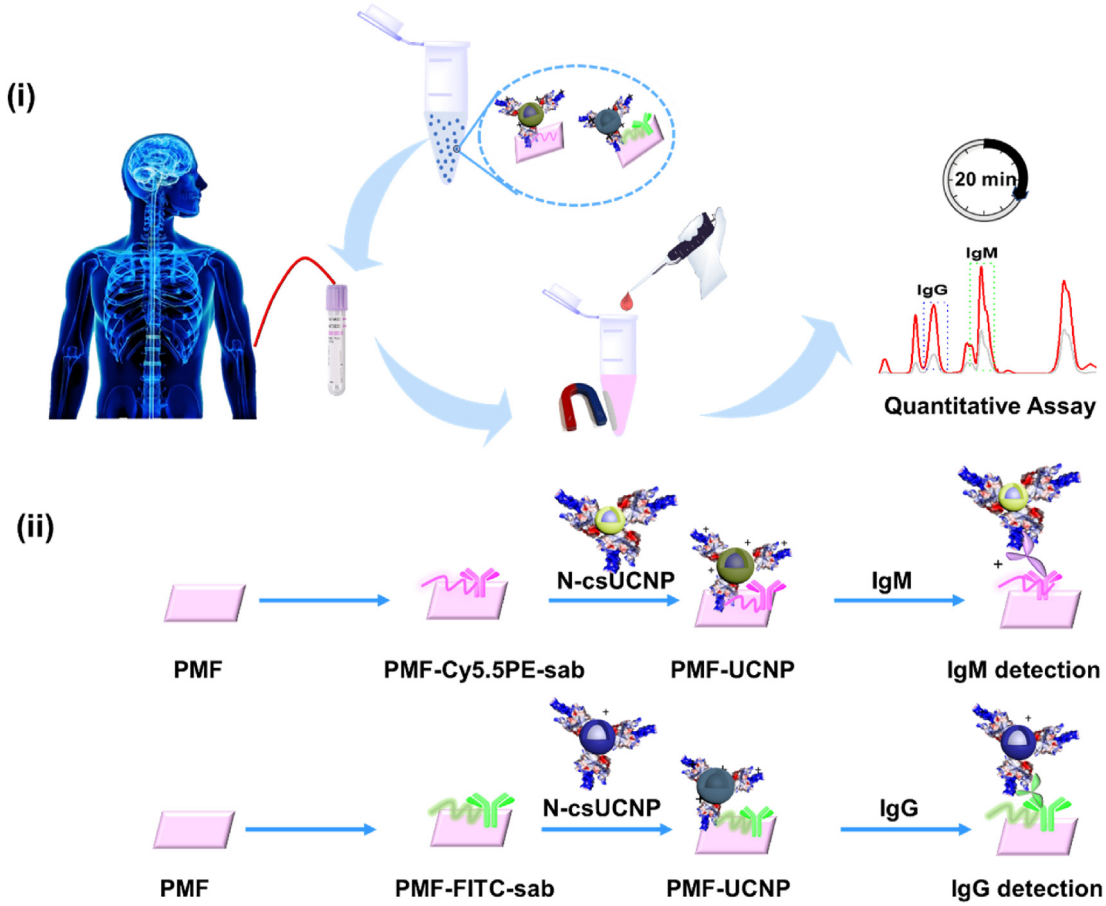

Scheme 1. Schematic illustration of the multicolor assay based on UCNPs, PMF-sab dye labeling for IgG and IgM detection. (i) Blood samples collected from COVID-19 patients are co-cultured with UCNP-based systems for multiple and specific detection. (ii) The detailed explanation of the detection. (ii)Magnetic PMF are co-cultured with Cy5.5 PE-anitIgM and FITC-antiIgG to form PMF-Cy5.5 PE-sab and PMF-FITC-sab as acceptors in the detection system. Abbreviations: FITC—-Fluorescein Isothiocyanate, Cy5.5-PE—1,2-dioleoyl-*sn*-glycero-3-phosphoethanolamine-*N*-(Cyanine 5.5) phycoerythrin (*PE*). sab — second antibody.

green emissions of Er^{3+} at 525 nm ($^2H_{11/2} \rightarrow {}^4I_{15/2}$) and 545 nm ($^4S_{3/2} \rightarrow {}^4I_{15/2}$) (Fig. 2a). The inert shell effectively prevents surface quenching of Yb^{3+} and Tm^{3+}/Er^{3+} in the core and provides protective effects after acidification. The OA-ligand free UCNPs display a high positive zeta potential (Fig. S2) and negligible absorbance in visible region (Fig. S3), endowing them with excellent water-solubility, dispersity and stability, thereby ensuring the possibility for further modification and detection. The successful modification of N protein on csUCNPs is demonstrated by zeta potential and FTIR results (Figs. S2 and S4). Moreover, the size increase from the original 50 nm (OA-UCNP) to 56 nm (*N*-csUCNP) (Fig. S5) further confirms the successful modification of *N*-protein on csUCNPs. As a proof of concept, we compared the changes in emission fluorescence changes in FITC-antiIgG and Cy5.5 PE-antiIgM in $NaYF_4$ and $NaGdF_4$ host matrices, respectively. As expected, the emissions of UCNPs in the blue and green regions were quenched by the dye-labeled antibody (Fig. 2d). The quenching efficiency (QE) was calculated as the relative luminescence change ratios as below:

$$\text{Qe}\ (\%) = \left(1 - \frac{I_a}{I}\right) \times 100 \tag{5}$$

where Ia and I represent the photoluminescence (PL) of csUCNPs with dyes (PMF) and csUCNPs alone, respectively. The QE of FITC-sab and Cy5.5 PE-sab were determined to be ~49.71 % at 475 nm and ~39.83 % at 542 nm, respectively. However, there is negligible FTIC emission in both $NaGdF_4$ and $NaYF_4$ host matrices (Fig. 2d–Fig. S6), which is different from a previous study of FITC and $NaGdF_4$ host [31]. This discrepancy may be attributed to the energy transfer from the triplet states to the ground states of FITC predominantly occurring through non-radiative pathways. Furthermore, the sensitizer and activators in $NaYF_4$ host matrix exhibit stronger PL intensity compared to $NaGdF_4$ nanocrystrals (Fig. 2b and c). Thus, the activators in $NaYF_4$ host matrix were chosen for the subsequent experiment. The cross-relaxation effect resulting from the co-doping of Tm^{3+} and Er^{3+} in UCNP, which was excluded from our experiment, should also be noted. Next, we sought to validate the performance of UCNPs and dye-labeled antibody on the detection of IgG and IgM although the trend was minimal (Fig. S7 a, c). Fortunately, the addition of both IgG and IgM have no discernible effect on the PL in the green and blue regions, ensuring the accuracy for the independent and mixed detection (Fig. S7 b, d). The results of our study indicate the possibility of simultaneously detecting IgG and IgM due to the absence of cross-interference throughout the detection process. This is advantageous as it allows for accurate and independent detection of both antibodies without any mutual influence on the fluorescence signals. Therefore, our findings suggest that the developed system has the potential to be utilized for the simultaneous detection of IgG and IgM in various applications.

3.4. Performance of PMF-UCNP nanosystems in IgG/IgM detection

Next, we utilize PMF-FITC-antiIgG and PMF-Cy5.5 PE-antiIgM specifically for capturing and recognizing IgG and IgM, respectively, and evaluate their performance in the detection of antibodies. Initially, the highly electropositive PMF (Fig. S2) were loaded with negatively charged dyes labeled sabs. Subsequently, BSA was used to block the PMF. There is

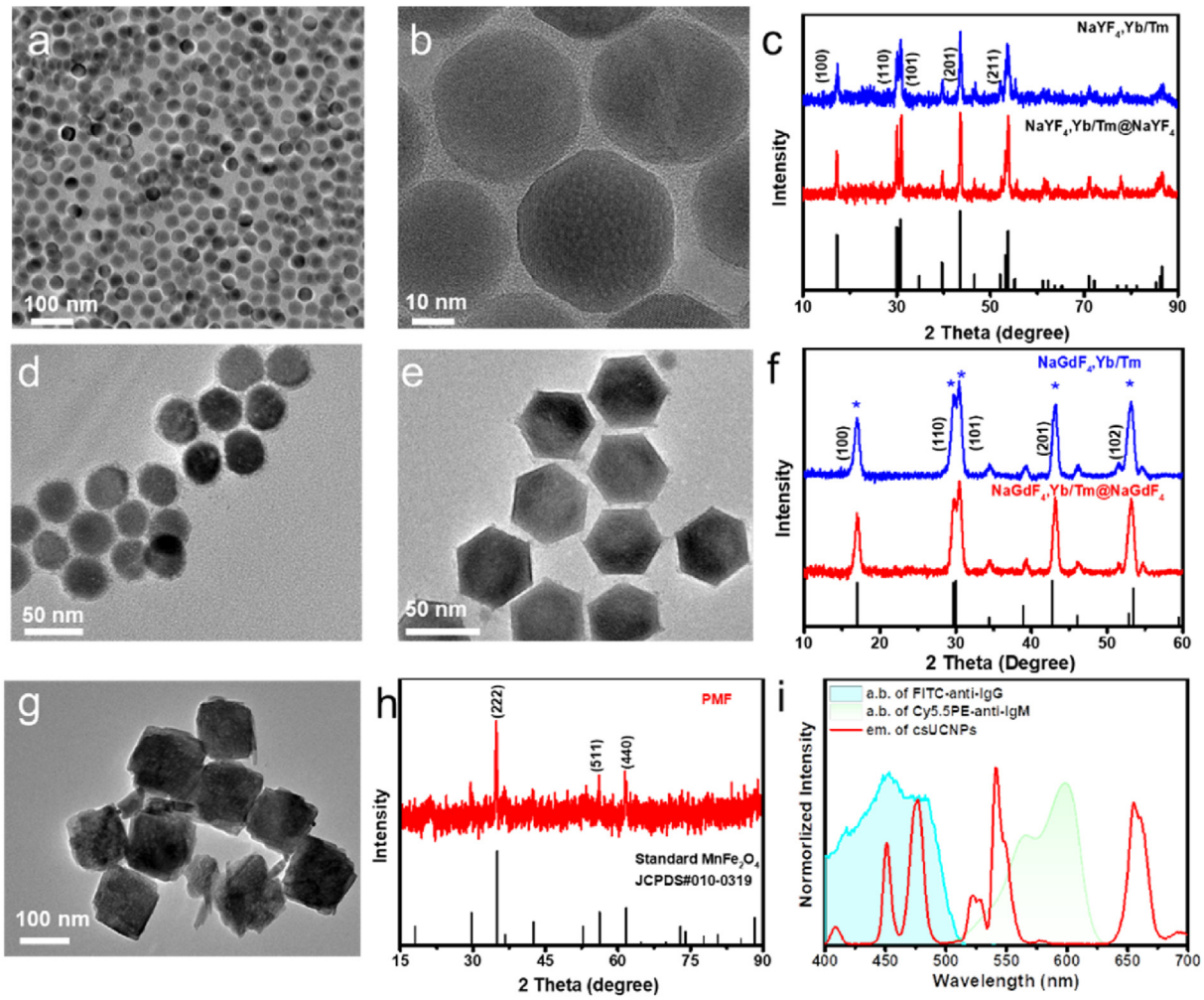

Fig. 1. Characterization of different nanocrystals. (a) TEM image of $NaYF_4$,Yb/Tm. (b) HRTEM image of $NaYF_4$,Yb/Tm@$NaYF_4$. (c) XRD spectra of $NaYF_4$,Yb/Tm and $NaYF_4$,Yb/Tm@$NaYF_4$. (d) TEM image of $NaGdF_4$,Yb/Tm. (e) TEM image of $NaGdF_4$,Yb/Tm@$NaGdF_4$. (f) XRD spectra of $NaGdF_4$,Yb/Tm and $NaGdF_4$,Yb/Tm@$NaGdF_4$. (g) TEM image of PMF NPs. (h) XRD spectrum of PMF NPs. (i) The emission luminescence spectrum of $NaYF_4$,Yb/Tm@$NaYF_4$ + $NaYF_4$,Yb/Er@$NaYF_4$ solution (red line), and the absorption spectra of FITC-*anti*-IgG (blue line) and Cy5.5 PE-*anti*-IgM (green line). Excitation intensity on UCNPs is 1 W cm^{-2}. The emission spectrum of UCNP overlaps well with the absorption spectra of the dye-labeled second antibody, illustrating a promising FRET effect.

an enhanced FRET effect occurring from the csUCNP to PMF-sab without the existence of the targets. Vivid confocal images before and after addition of antibodies to the biodetection systems could be observed in Fig. 3 a, b. The PL of *N*-csUCNPs is recovered with the appearance of IgG (blue) and IgM (green). The PL intensity increases with the increasing concentrations of IgG at 475 nm, and a significant dose-responsive curve was identified, illustrating the assays were promising in detecting of IgG at this range (Fig. 3 c and d). By further evaluating the specificity of detecting IgM at 542 nm, the PL in 542 nm recovers with the increasing concentrations of IgM, revealing a sigmoidal curve (Fig. 3 e, f). Importantly, the inclusion of PMF in the detection system amplify the signal and enhance the detection sensitivity compared to Fig. 2. This improvement can be attributed to the ability of PMF to capture and enrich the target antibodies. Additionally, the presence of PMF-sab led to a significant increase of quenching efficiency (Qe) due to their large surface area and high surface energy transfer.

3.5. *Theoretical modeling and simulation*

The basic model for the energy transfer from csUCNPs to dye-labeled sab and PMF-sab are shown in Fig. 4a, the addition of targets significantly increases the distance between the csUCNPs and PMF-sab, thereby blocking the FRET process and resulting in the recovery of PL. To further understand the detailed influences of PMF on the PL of csUCNPs, we performed a classical phenomenological model using the finite-difference time-domain (FDTD) method. This involves numerical integrating the full vectorial Maxwell equations. The specific simulation process were carried out as previously described [30]. In brief, we conducted a simulation to analyze the distribution of Er^{3+} ions in *N*-csUCNP when in contact with the PMF. The initial distance between Er^{3+} to PMF was estimated to 8 nm (From the DLS data). The quenching factor (η/η_0) of each Er^{3+} ion is represented by the color bar in Fig. 4b. The simulation results include 2 models, one without IgM (left) and with target IgM (right). We observed a strong quenching effect at the north hemisphere of csUCNPs when a PMF NP was present on one side, resulting in a Qe value of approximately 0.5. However, after the addition of *anti*-SARS-CoV-2 IgM, most of the Er^{3+} ions were not affected by the PMF due to a significant increase in the distance between PMF and UCNPs (above 23 nm). This leads to a lower quenching efficiency (Qe~0.1, as shown in Fig. 4c). These results demonstrate the enhanced Qe and improved limit of detection (LOD) achieved through the introduction of PMF. It is important to note that the calculations were solely based on the inorganic PMF and csUCNP, considering the dye's effects. Additionally, the decay rates before and after the addition of PMF were evaluated in Fig. 4d and e. As anticipated, the presence of PMF resulted in a decrease in the lifetime of both $NaYF_4$,Yb/Tm@$NaYF_4$ and $NaYF_4$,Yb/Tm@$NaYF_4$. Notably, the

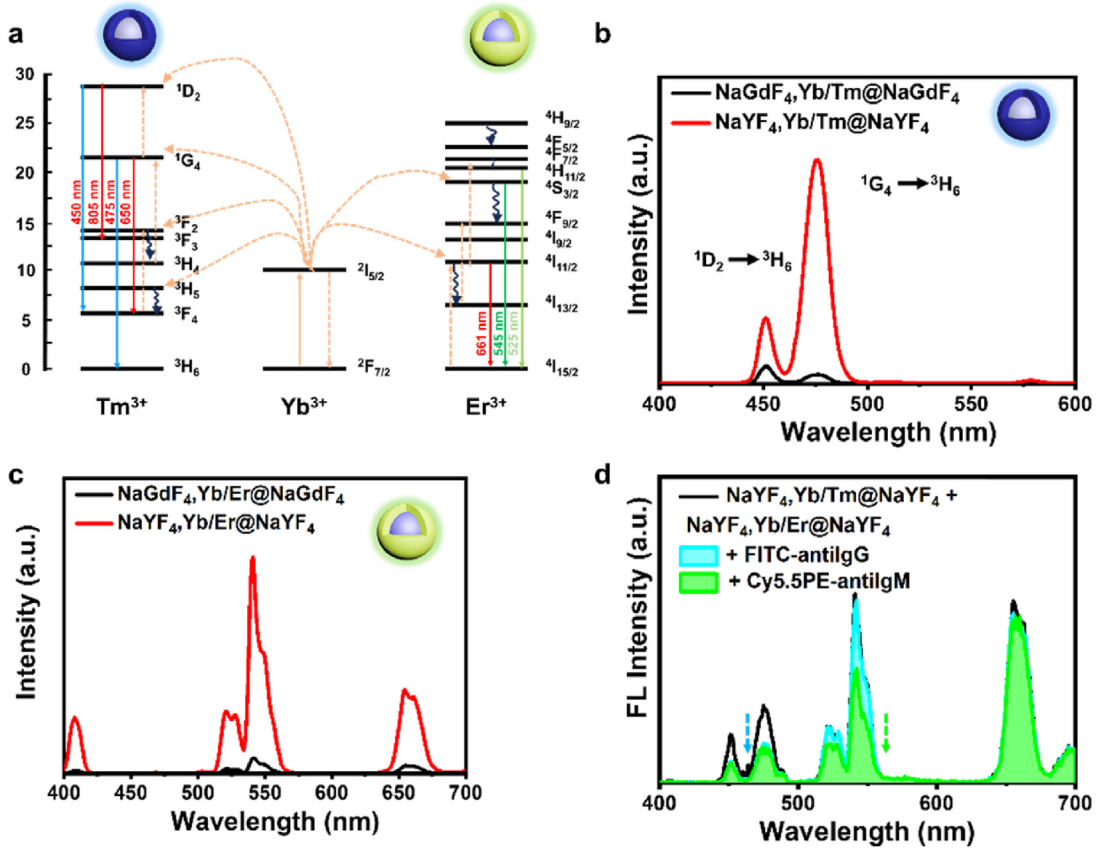

Fig. 2. The possible mechanism of multicolor UCNP-based systems on detecting IgG and IgM. (a) Mechanism of the Tm^{3+}, Er^{3+} and Yb^{3+} upconversion process in the UCNPs under 980 nm excitation. (b) UCL spectra of $NaGdF_4$,Yb/Tm@$NaGdF_4$ and $NaYF_4$,Yb/Tm@$NaGdF_4$. (b) UCL spectra of UCL spectra of $NaGdF_4$,Yb/Er@$NaGdF_4$ and $NaYF_4$,Yb/Er@$NaGdF_4$. The $NaYF_4$-based UCNPs exhibited stronger luminescence intensity than $NaGdF_4$-based UCNPs。 (d) The influence of FITC-antiIgG and Cy5.5 PE-antiIgM on the emission spectra of *N*–$NaYF_4$,Yb/Tm@$NaYF_4$ and *N*–$NaYF_4$,Yb/Er@$NaYF_4$.

participation of PMF contributes to a faster decay compare to the dye-labeled sab. Specifically, there are significant changes in the luminescence lifetime from $\tau = 536$ μs to $\tau = 460$ μs at 475 nm, and an even stronger effect was observed at 542 nm, with a decrease from $\tau = 186$ μs to $\tau = 120$ μs These findings confirm the enhanced FRET between UCNPs and PMF, which aligns with the theoretical simulation results.

3.6. Simultaneous detection of IgG and IgM

We sought to evaluate the performance of the multicolor assay in detecting IgG and IgM. As shown in Fig. 5a, the emission intensity of the csUCNPs recovers well with increasing amounts of IgG and IgM at 475 nm and 542 nm, highlighting the advantages of multiple narrow emission in detecting multiple targetes. Specifically, for IgG detection, the recovered PL at 475 nm follows sigmoidal curves with dose-response characteristics from 4 to 2000 pg mL^{-1} (Fig. 5 b). In the region 8–250 pg mL^{-1}, a linear equation of y = 0.083 + 1.0765 at 475 nm (Fig. S8) was observed. For IgM detection, the recovered emission can be fitted to the linear equation, y = 0.6835X+0.02117 (X = Log_{10} [concentration]) at 542 nm. For comparison, we also investigate antibody the detection without PMF (Fig. 5 d, e, f), a minor enhancement of PL was observed with the increased amounts of IgG and IgM, represented by equations y = 0.1083X+1.008 at 475 nm and y = 0.0997X+1.007 at 542 nm, respectively, representing a similar linear trend in blue and green regions. The limits of detection (LODs) in PMF-assisted biodetection system for IgG and IgM are calculated to be 13.49 pg mL^{-1} and 15.50 pg mL^{-1}, namely 89 fmol L^{-1} and 19.4 fmol L^{-1}, respectively. In contrast, the LODs for IgG and IgM in the system without PMF are 5.62 ng mL^{-1} and 7.56 ng mL^{-1}, respectively, demonstrating a 416-folds and 487-folds improvement in detection sensitivity due to the introduction of PMF./ Furthermore, we evaluate the feasibility of our UCNP-based biodetection system for real plasma detection. There are no distinct changes in PL spectra among negative serum (undiluted), human serum albumin (HSA) solution (1 mg/mL) and ddH_2O, illustrating negligible influence of serum components on the detection (Fig. S9). Moreover, we employed different antibodies (*anti*-HIV-IgG, *anti*-HIN1-IgG, IgA) to test the specificity of the detection system. As expected, there was negligible PL changes after addition of these antibodies with different concentrations, illustrating the high specificity of the detection.

3.7. Clinical detection of IgG and IgM

Finally, we evaluate their performance for clinical blood sample detection from COVID-19-negative patients and vaccinated patients. Here, 10 μL blood were mixed with PMF-sab and two antibodies (*anti*-SARS-CoV-2 IgG and IgM) were analyzed simultaneously using the multiplex UCNP-based nanosystems. The very small amounts of blood could also be got from fingertip, like the blood volume for glucometer. As shown in Fig. 6a and b, the detection system can efficiently distinguish negative and positive samples as well as quantify the contents of IgG and IgM. Normally, the contents of IgG and IgM varied at different intervals after vaccinated and their detailed contents are especially important for assessing the efficacy of the vaccines and the corresponding epidemic prevention policy. Our results illustrate that the average contents of *anti*-CoV-2 IgG decreased significantly after vaccinated for 1 year, which are still higher than the negative samples. By contrast, there was no difference in IgM between the vaccinated samples (above 1 year) and negative samples. In addition, as ELISA method (cost more than 4 h, Fig. 6c) is a

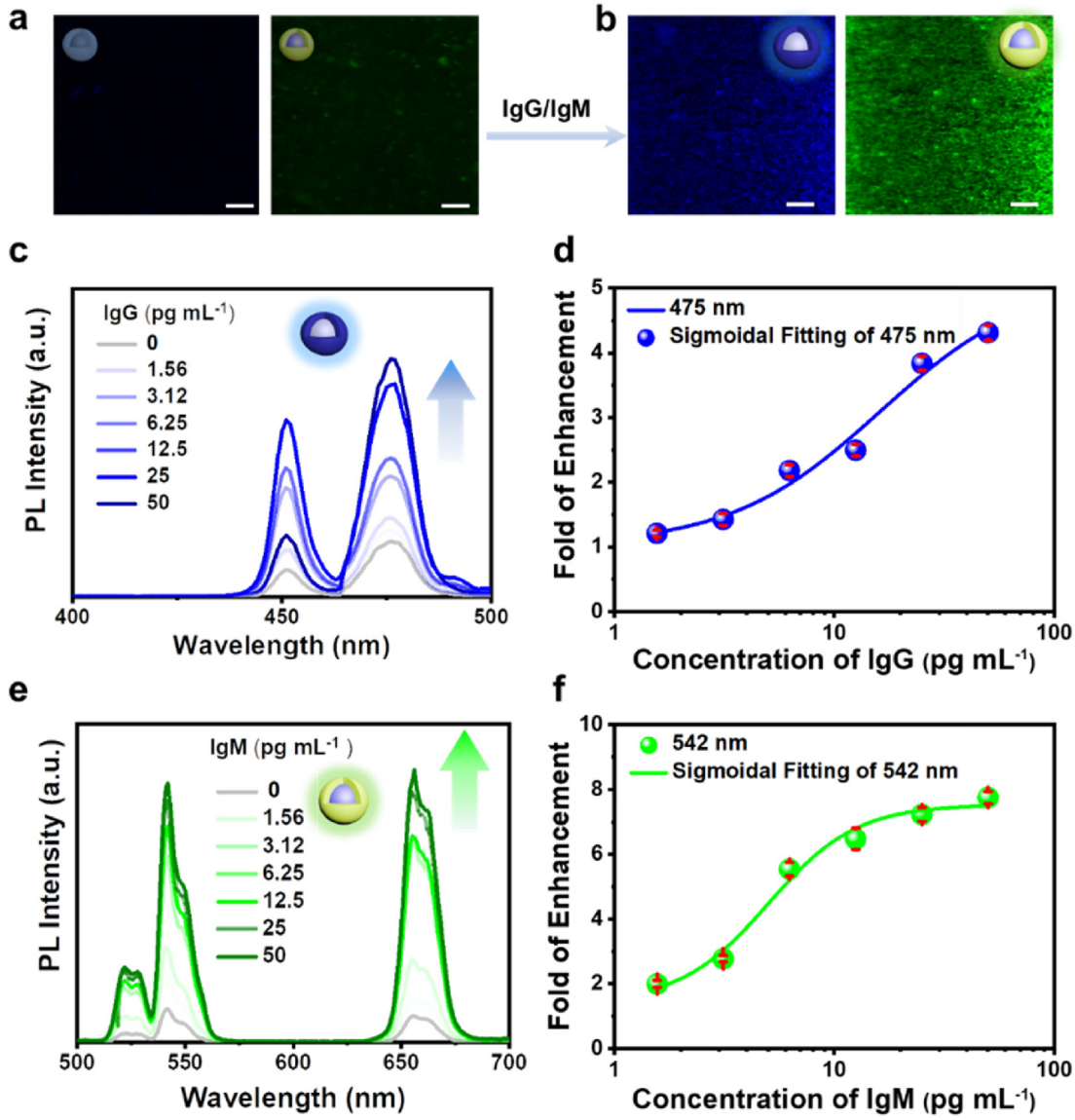

Fig. 3. Analysis and quantification of IgG and IgM using PMF-sab. Confocal fluorescence images of (a) $NaYF_4$,Yb,Tm@$NaYF_4$ + PMF-sab and $NaYF_4$,Yb,Er@$NaYF_4$ + PMF-sab; and (b) $NaYF_4$,Yb,Tm@$NaYF_4$ + PMF-sab + IgG and $NaYF_4$,Yb,Er@$NaYF_4$ + PMF-sab + IgM; The blue and green luminescence are emitted by $NaYF_4$,Yb,Tm@$NaYF_4$ and $NaYF_4$,Yb,Er@$NaYF_4$ after addition of IgG and IgM (Ex. = 980 nm); (c) PL changes of $NaYF_4$,Yb,Tm@$NaYF_4$ with gradient concentrations of IgG; (d) Analytical dose-response curves of IgG from (c); (e) PL changes of $NaYF_4$,Yb,Er@$NaYF_4$ with gradient concentrations of IgM; (f) Analytical dose-response curves of IgM from (e); each value is the mean ± standard deviation (n = 3 in each group).

standard method for antibody detection, the IgG and IgM in blood are further verified using ELISA method (Fig. 6 d, e), which closely matched with the contents of IgG and IgM (Fig. 6 f, g. $R^2 = 0.998$ and $R^2 = 0.997$, respectively). Notably, our detection for IgG and IgM could be finished within 20 min simultaneously. While for ELISA, the detection procedures of IgG and IgM are separately and the whole processes for IgG/IGM need to take about 4 h, which is a great waste of time and resources. In addition, the sensitivity is much higher than previous reported IgM/IgG method [32]. The results illustrate our biosystem achieved high accuracy to detect clinical antibodies, which could be employed to evaluate the effect of vaccines at different intervals.

4. Conclusions

In this work, we have fabricated csUCNP and PMF-dye-sab biosensor for rapid and ultrasensitive detection of COVID-19 IgM and IgG. By tuning the multi-color of the csUCNPs, the IgG and IgM are specifically recognized in blue and green regions, respectively. Importantly, the introducing of PMF into the detection system enable to efficiently capture the antibodies and improve the detection sensitivity of IgG and IgM by 416-folds and 487-folds. We have performed theoretical modeling and simulation to deepen the understanding of our proposed detection scheme and the working principle has been investigated by FDTD. Clinical blood sample from COVID-19-negative patients and vaccinated patients are employed to evaluate the performance of our biosensor and prove the effectiveness in practical application. The whole detection could be finished within 20 min with high accuracy and specificity. The developed homogeneous diagnostic method based on blocking FRET effect between UCNPs and dyes is capable of detecting COVID-19 antibodies in clinical blood specifically and conveniently, which is promising for the diagnosis and evaluation of the effect of vaccines and infections. This design is hopefully to expand to antigen and other antibody detection. In addition to the merits of the established method, there is still room for improvement, particularly in the development of high

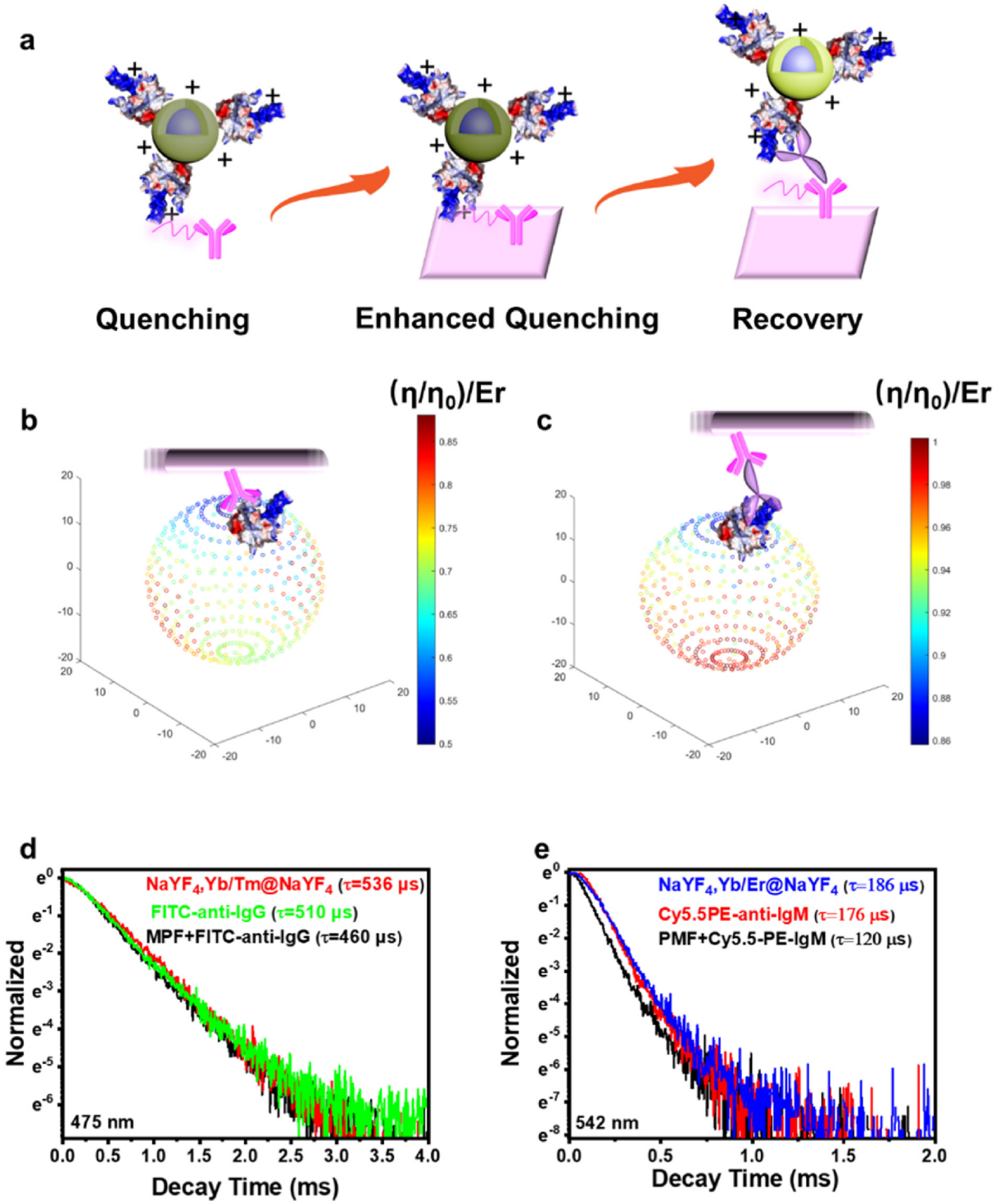

Fig. 4. Simulation analysis of quenching factors between csUCNP and PMF. (a) Schematic illustration of the quenching and recovery process PL. Simulated distribution of the quenching factor of each individual Er^{3+} ion (η/η0) in csUCNP with PMF in one side (**b**) without IgM and (**c**) with IgM, the simulation exclusive of the organic dye. Normalized luminescence curves at of (**d**) $NaYF_4$,Yb/Tm@$NaYF_4$, $NaYF_4$,Yb/Tm@$NaYF_4$ + FITC-sab, and $NaYF_4$,Yb/Tm@$NaYF_4$ + PMF-FITC-sab at 475 nm and (**e**) $NaYF_4$,Yb/Er@$NaYF_4$, $NaYF_4$,Yb/Er@$NaYF_4$ + Cy5.5 PE-sab, and $NaYF_4$,Yb/Er@$NaYF_4$ + PMF-Cy5.5 PE-sab at 542 nm.

throughput testing based-on multicolor detection system. In future study, we will focus on the development of a multichannel and high-throughput diagnostic platform to address these issues.

Credit author statement

All authors have participated the work. L.L: conceived the concept, conducted the experiments, and wrote the manuscript. collect the clinical samples and analyzed them. Y. L: collect the clinical samples and analyzed them. X. L: carried out the experiment, analyzed the data and revised the manuscript. S. P: carried out the experiment, analyzed the data and revised the manuscript. M. S: carried out the experiment, analyzed the data and revised the manuscript. M. W: carried out the experiment, analyzed the data and revised the manuscript. F. W:

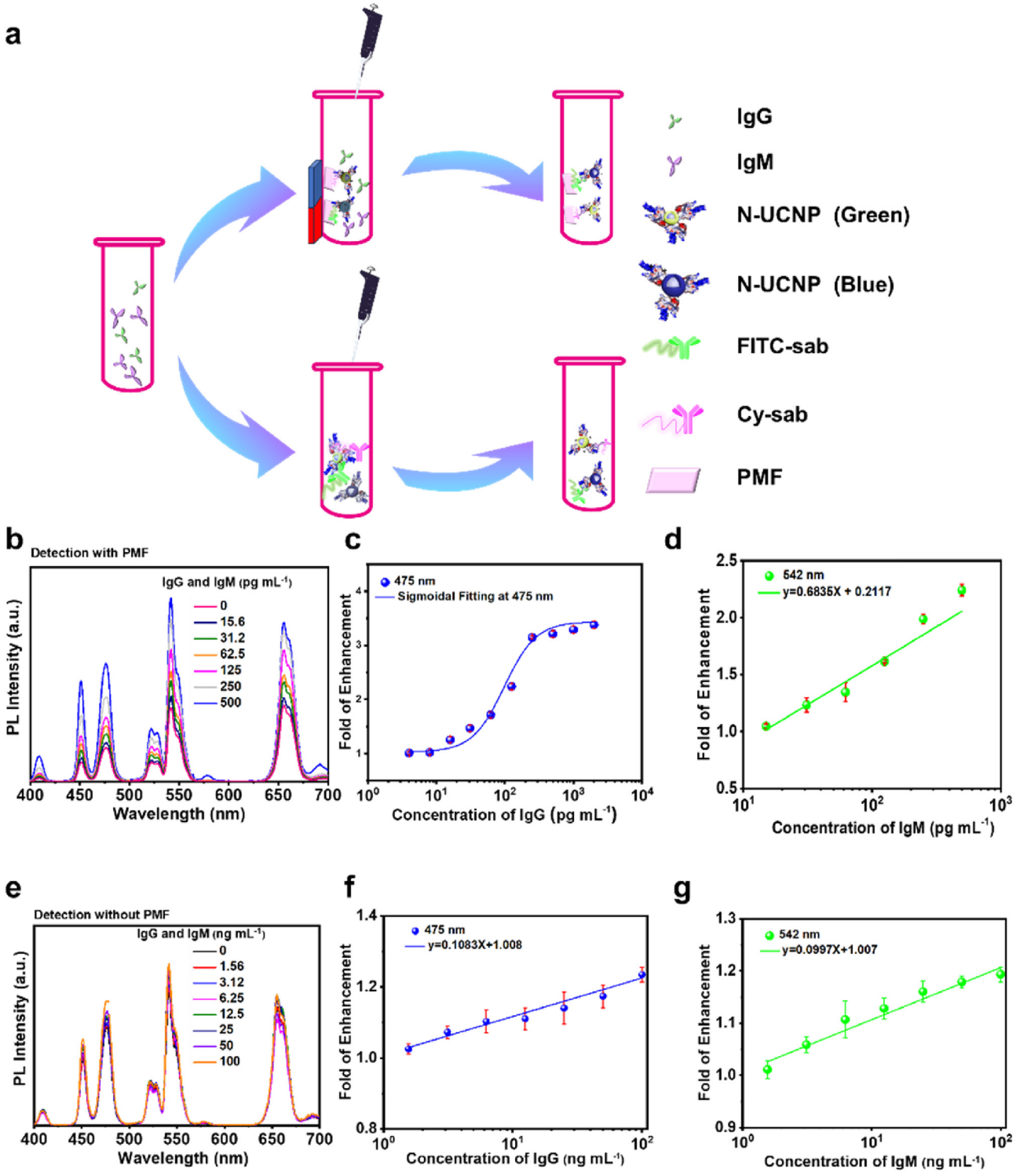

Fig. 5. Performance of the multiplex biosystems for simultaneous detection of IgG and IgM. (a) Scheme of detection process with or without PMF. **(b)** UCL changes of csUCNP ($NaYF_4$,Yb,Tm@$NaYF_4$ + $NaYF_4$,Yb,Er@$NaYF_4$) after addition of different concentrations of IgG and IgM with PMF. Analytical dose-response curves for detection of **(c)** IgG based on PMF-FITC-fantiIgG and csUCNPs, and **(d)** IgM based on PMF-Cy5.5 PE-antiIgM and UCNPs. **(e)** Emission spectra of csUCNP with different concentration of IgG and IgM only with dye-labeled sab. PL changes at **(f)** 475 nm for IgG detection, and **(g)** 542 nm nm for IgM detection. Each value is the mean ± standard deviation ($n = 3$ in each group).

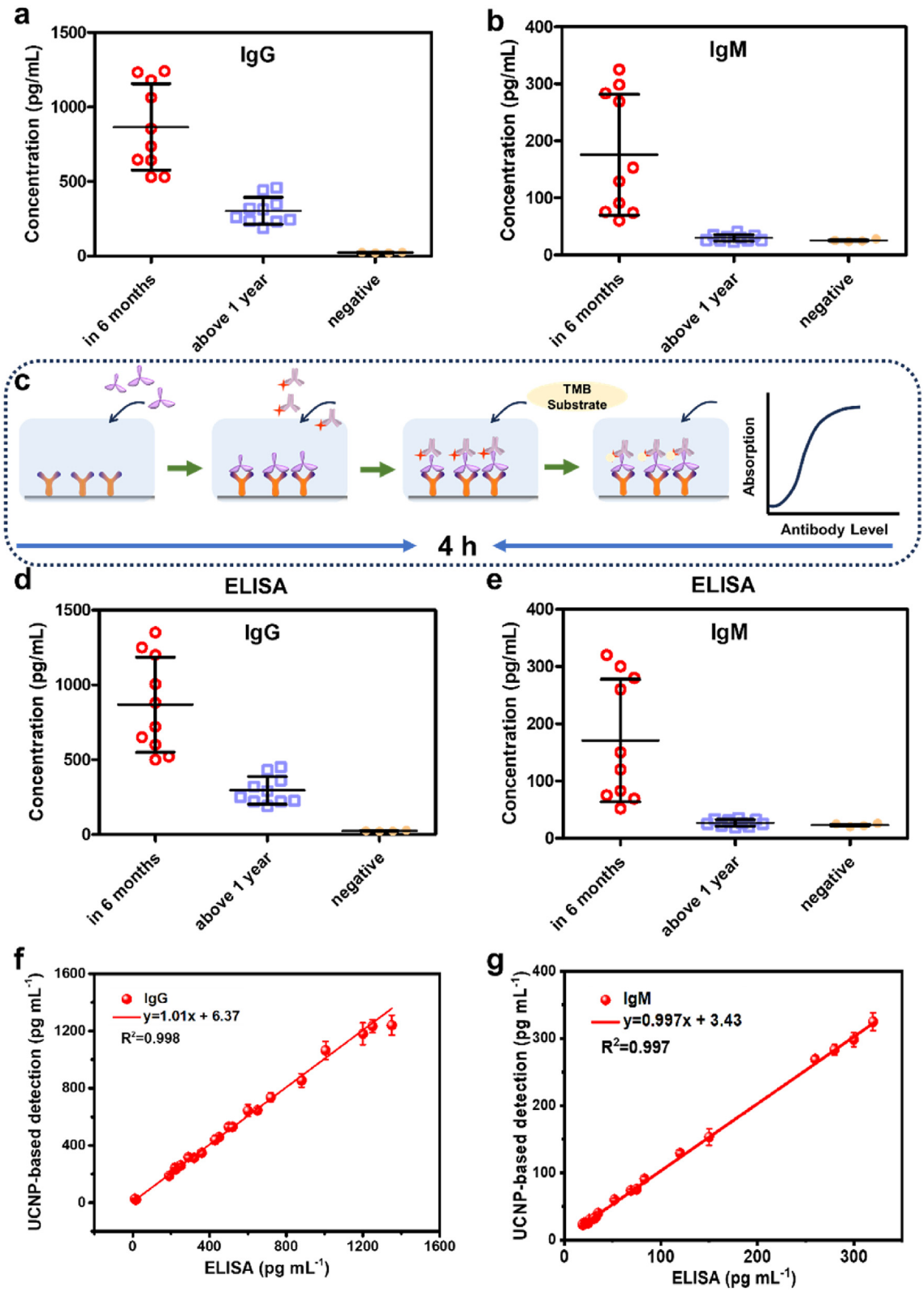

Fig. 6. Detecting of clinical samples. UCNP-based assay for evaluating of the contents of (**a**) *anti*-SARS-CoV-2 IgG and (**b**) *anti*-SARS-CoV-2 IgM in negative and vaccinated human blood. ELISA for evaluating of the contents of (**c**) Scheme illustration of ELISA detection procedure. ELISA-based assay for assessing of the contents of (**d**) *anti*-SARS-CoV-2 IgG and (**e**) *anti*-SARS-CoV-2 IgM in negative and vaccinated human blood. Comparison of established UCNP-based method with ELISA in (**f**) IgG and (**g**) IgM.

supported the experiment and the idea. M. Y: supported the experiment and the idea. J. H. designed, supported the work, supervised the projects and revised the manuscript.

Declaration of competing interest

The authors declare that they have no known competing financial interests or personal relationships that could have appeared to influence the work reported in this paper.

Acknowledgement

The work described in this paper was supported by a grant from the Research Grants Council of the Hong Kong Special Administrative Region, China (Project No. CRF No. PolyU C5110-20G) and PolyU Internal Research Fund (1-CD4S, 1-W18E, 1-CE0H).

Appendix A. Supplementary data

Supplementary data to this article can be found online at https://doi.org/10.1016/j.smaim.2023.12.003.

References

[1] C.B. Creech, S.C. Walker, R.J. Samuels, SARS-CoV-2 vaccines, JAMA 325 (13) (2021) 1318–1320.
[2] C. Liao, X. Chen, Y. Fu, Salivary analysis: an emerging paradigm for non-invasive healthcare diagnosis and monitoring, Interdiscipl. Med. 1 (3) (2023) e20230009.
[3] A.E. Muruato, C.R. Fontes-Garfias, P. Ren, M.A. Garcia-Blanco, V.D. Menachery, X. Xie, P.-Y. Shi, A high-throughput neutralizing antibody assay for COVID-19 diagnosis and vaccine evaluation, Nat. Commun. 11 (1) (2020) 4059.
[4] R.W. Peeling, D.L. Heymann, Y.-Y. Teo, P.J. Garcia, Diagnostics for COVID-19: moving from pandemic response to control, Lancet 399 (10326) (2022) 757–768.
[5] H. Qi, B. Liu, X. Wang, L. Zhang, The humoral response and antibodies against SARS-CoV-2 infection, Nat. Immunol. 23 (7) (2022) 1008–1020.
[6] Q.-X. Long, B.-Z. Liu, H.-J. Deng, G.-C. Wu, K. Deng, Y.-K. Chen, P. Liao, J.-F. Qiu, Y. Lin, X.-F. Cai, Antibody responses to SARS-CoV-2 in patients with COVID-19, Nat. Med. 26 (6) (2020) 845–848.
[7] K.K.-W. To, O.T.-Y. Tsang, W.-S. Leung, A.R. Tam, T.-C. Wu, D.C. Lung, C.C.-Y. Yip, J.-P. Cai, J.M.-C. Chan, T.S.-H. Chik, Temporal profiles of viral load in posterior oropharyngeal saliva samples and serum antibody responses during infection by SARS-CoV-2: an observational cohort study, Lancet Infect. Dis. 20 (5) (2020) 565–574.
[8] D.F. Robbiani, C. Gaebler, F. Muecksch, J.C. Lorenzi, Z. Wang, A. Cho, M. Agudelo, C.O. Barnes, A. Gazumyan, S. Finkin, Convergent antibody responses to SARS-CoV-2 in convalescent individuals, Nature 584 (7821) (2020) 437–442.
[9] T.F. Rogers, F. Zhao, D. Huang, N. Beutler, A. Burns, W.-t. He, O. Limbo, C. Smith, G. Song, J. Woehl, Isolation of potent SARS-CoV-2 neutralizing antibodies and protection from disease in a small animal model, Science (New York, N.Y.) 369 (6506) (2020) 956–963.
[10] H. Liu, A. Yang, J. Song, N. Wang, P. Lam, Y. Li, H.K.-w. Law, F. Yan, Ultrafast, sensitive, and portable detection of COVID-19 IgG using flexible organic electrochemical transistors, Sci. Adv. 7 (38) (2021) eabg8387.
[11] Z.Z. Rashid, S.N. Othman, M.N.A. Samat, U.K. Ali, K.K. Wong, Diagnostic performance of COVID-19 serology assays, Malays. J. Pathol. 42 (1) (2020) 13–21.
[12] F. Amanat, D. Stadlbauer, S. Strohmeier, T.H. Nguyen, V. Chromikova, M. McMahon, K. Jiang, G.A. Arunkumar, D. Jurczyszak, J. Polanco, A serological assay to detect SARS-CoV-2 seroconversion in humans, Nat. Med. 26 (7) (2020) 1033–1036.
[13] J. Xiang, M. Yan, H. Li, T. Liu, C. Lin, S. Huang, C. Shen, Evaluation of enzyme-linked immunoassay and colloidal gold-immunochromatographic assay kit for detection of novel coronavirus (SARS-Cov-2) causing an outbreak of pneumonia (COVID-19), medRxiv (2020).
[14] W. Liu, G. Kou, Y. Dong, Y. Zheng, Y. Ding, W. Ni, W. Wu, S. Tang, Z. Xiong, Y. Zhang, Clinical application of chemiluminescence microparticle immunoassay for SARS-CoV-2 infection diagnosis, J. Clin. Virol. 130 (2020) 104576.
[15] H. Kang, X. Wang, M. Guo, C. Dai, R. Chen, L. Yang, Y. Wu, T. Ying, Z. Zhu, D. Wei, Ultrasensitive detection of SARS-CoV-2 antibody by graphene field-effect transistors, Nano Lett. 21 (19) (2021) 7897–7904.
[16] S. Yan, K.Z. Ahmad, A.R. Warden, Y. Ke, N. Maboyi, X. Zhi, X. Ding, One-pot pre-coated interface proximity extension assay for ultrasensitive co-detection of anti-SARS-CoV-2 antibodies and viral RNA, Biosens. Bioelectron. 193 (2021) 113535.
[17] D. Najjar, J. Rainbow, S. Sharma Timilsina, P. Jolly, H. De Puig, M. Yafia, N. Durr, H. Sallum, G. Alter, J.Z. Li, A lab-on-a-chip for the concurrent electrochemical detection of SARS-CoV-2 RNA and anti-SARS-CoV-2 antibodies in saliva and plasma, Nat. Biomed. Eng. 6 (8) (2022) 968–978.
[18] F. Wang, D. Banerjee, Y. Liu, X. Chen, X. Liu, Upconversion nanoparticles in biological labeling, imaging, and therapy, Analyst 135 (8) (2010) 1839–1854.
[19] B. Gu, Q. Zhang, Recent advances on functionalized upconversion nanoparticles for detection of small molecules and ions in biosystems, Adv. Sci. 5 (3) (2018) 1700609.
[20] M. Song, M. Yang, J. Hao, Pathogenic virus detection by optical nanobiosensors, Cell Rep. Phy.l Sci. 2 (1) (2021) 100288.
[21] L. Li, M. Song, X. Lao, S.-Y. Pang, Y. Liu, M.-C. Wong, Y. Ma, M. Yang, J. Hao, Rapid and ultrasensitive detection of SARS-CoV-2 spike protein based on upconversion luminescence biosensor for COVID-19 point-of-care diagnostics, Mater. Des. (2022) 111263.
[22] Y. Ma, M. Song, L. Li, X. Lao, M.C. Wong, J. Hao, Advances in Upconversion Luminescence Nanomaterial-based Biosensor for Virus Diagnosis, Wiley Online Library, Exploration, 2022 20210216.
[23] M. Song, Y. Ma, L. Li, M.-C. Wong, P. Wang, J. Chen, H. Chen, F. Wang, J. Hao, Multiplexed detection of SARS-CoV-2 based on upconversion luminescence nanoprobe/MXene biosensing platform for COVID-19 point-of-care diagnostics, Mater. Des. (2022) 111249.
[24] Q. Su, W. Feng, D. Yang, F. Li, Resonance energy transfer in upconversion nanoplatforms for selective biodetection, Accounts Chem. Res. 50 (1) (2017) 32–40.
[25] V. Muhr, C. Würth, M. Kraft, M. Buchner, A.J. Baeumner, U. Resch-Genger, T. Hirsch, Particle-size-dependent förster resonance energy transfer from upconversion nanoparticles to organic dyes, Anal. Chem. 89 (9) (2017) 4868–4874.
[26] H.M. Luong, T.A. Ngo, M.T. Pham, Y. Zhao, G.K. Larsen, T.-Q. Nguyen, T.D. Nguyen, Ultra-fast and sensitive magneto-optical hydrogen sensors using a magnetic nano-cap array, Nano Energy 109 (2023) 108332.
[27] X. Huang, Y. Liu, B. Yung, Y. Xiong, X. Chen, Nanotechnology-enhanced no-wash biosensors for in vitro diagnostics of cancer, ACS Nano 11 (6) (2017) 5238–5292.
[28] M.K. Tsang, Y.T. Wong, T.H. Tsoi, W.T. Wong, J. Hao, Upconversion luminescence sandwich assay for detection of influenza H7 subtype, Adv. Healthcare Mater. 8 (18) (2019) 1900575.
[29] T. Gao, Y. Gao, X. Liu, Z. Nie, H. Sun, K. Lin, H. Peng, S. Wang, Identification and functional analysis of the SARS-COV-2 nucleocapsid protein, BMC Microbiol. 21 (1) (2021) 58.
[30] D. Mendez-Gonzalez, S. Melle, O.G. Calderon, M. Laurenti, E. Cabrera-Granado, A. Egatz-Gomez, E. Lopez-Cabarcos, J. Rubio-Retama, E. Diaz, Control of upconversion luminescence by gold nanoparticle size: from quenching to enhancement, Nanoscale 11 (29) (2019) 13832–13844.
[31] R. Deng, J. Wang, R. Chen, W. Huang, X. Liu, Enabling Förster resonance energy transfer from large nanocrystals through energy migration, J. Am. Chem. Soc. 138 (49) (2016) 15972–15979.
[32] R. Chen, C. Ren, M. Liu, X. Ge, M. Qu, X. Zhou, M. Liang, Y. Liu, F. Li, Early Detection of SARS-CoV-2 seroconversion in humans with aggregation-induced near-infrared emission nanoparticle-labeled lateral flow immunoassay, ACS Nano 15 (5) (2021) 8996–9004.